A Spherical Coil Array for the Calibration of Whole-Head Magnetoencephalograph Systems

Yoshiaki Adachi, *Member, IEEE*, Daisuke Oyama, *Member, IEEE*, Masanori Higuchi, and Gen Uehara, *Member, IEEE*

***Abstract*— We proposed a spherical coil array for determining the positions, orientations, and sensitivities of the magnetometers for whole-head magnetoencephalograph (MEG) systems. The coil array comprises 16 concentric and symmetrically oriented circular coils with a diameter of 150 mm, which is larger than those of conventional calibration coil arrays, such as 5 or 60 mm. The accuracy of the calibration was expected to improve because the relative mechanical errors in machining and assembly could be reduced when the coil diameter was increased. Moreover, we also proposed a method to estimate the uncertainties in calibration, and it was demonstrated that the sensor parameters of each sensor were successfully obtained with uncertainties using a spherical calibration coil array. Additionally, the accuracy of the calibration was evaluated using a dry-type MEG phantom, and as expected, it was found that the accuracy was improved from that of a conventional calibration coil array composed of an assembly of multiple three-axis bobbins.**

***Index Terms*— Calibration, magnetoencephalography, magnetometers, superconducting quantum interference devices (SQUIDs), uncertainty estimation.**

I. Introduction

MAGNETOENCEPHALOGRAPH (MEG) is a promising tool to non-invasively investigate brain functions [1]. An array of multiple highly sensitive magnetic flux sensors arranged along the surface of the head captures the distribution of weak magnetic fields accompanied by electrical neural activity in the brain. The neural current distribution in the brain is reconstructed using magnetic source analysis based on the obtained magnetic field distribution. Subsequently, MEG non-invasively provides vital functional information about the brain as the transition of the reconstructed current distribution is superimposed on the anatomical information from magnetic resonance imaging.

The magnetic field generated from brain activity is quite small; thus, magnetic flux sensors with superconducting quantum interference devices (SQUIDs) are practically employed for detecting MEG signals. The position, orientation, and sensitivity of each SQUID sensor must be determined precisely to accurately localize magnetic sources from the obtained magnetic field distribution. However, it is rather difficult to precisely determine these values for the following two reasons. First, the SQUID sensor array is made of grass fiber reinforced plastic (GFRP), because it must be non-magnetic; hence it is inevitably strained at cryogenic temperatures. The coefficient of thermal expansion of GFRP is approximately 10^{-5}/K. The temperature difference between the room and superconducting temperature is approximately 300 K. The dimensions of the MEG cryostat are 1 m. In this case, the position shift from the designed values could be roughly estimated as 3 mm, which is not negligible. According to Kawakatsu et al. [2], the position and orientation of the sensors unexpectedly shift from their designed values after cooling. Second, the sensitivity and orientation of a SQUID sensor are influenced by the variation in the SQUID chips of sensors and the parasitic inductance of the pick-up coil coupled with the SQUID chip, particularly in the case of sensors with wire-wound gradiometric pick-up coils. Therefore, the calibration of sensors after cooling is crucial for obtaining accurate results in magnetic source analysis.

An array of coils that fits into the helmet-shaped sensor array of a whole-head MEG system is often applied to generate reference magnetic fields to determine the effective position and orientation of SQUID sensors after cooling [3], [4], [5], [6], [7]. The reference magnetic field signal can be theoretically calculated by assuming that the SQUID sensor is placed at a specific point. The position and orientation of the sensor were determined via a numerical search to minimize the difference between the theoretical magnetic field signals and the measured magnetic field signals. The sensitivity of the sensor was estimated based on the intensity of the excitation current and the detected reference magnetic field signals. The procedure for determining the sensor parameters is called sensor calibration. The precision of the coil array is a crucial factor in accurate calibration. In our previous study, we utilized an array of coils composed of multiple three-axis coil bobbins to calibrate the MEG sensor array and demonstrated that the calibration accuracy was enhanced by precise measurement of the coil geometry using an X-ray computational tomography (CT) [7]. When the diameter of the coil is increased, the relative error of the coil shape from the designed values can be smaller than that of the conventional calibration coil array, and a more accurate calibration is expected.

Another approach for SQUID sensor calibration after cooling is to apply large square Helmholtz-like coils placed outside the cryostat to generate reference magnetic fields [8], [9], [10]. Yang et al. [11] proposed a special bi-planar coil designed

Manuscript received 5 December 2022; revised 6 March 2023; accepted 19 March 2023. Date of publication 10 April 2023; date of current version 24 April 2023. The Associate Editor coordinating the review process was Dr. Yuan Gao. *(Corresponding author: Yoshiaki Adachi.)*

The authors are with the Applied Electronics Laboratory, Kanazawa Institute of Technology, Nonoichi, Ishikawa 921-8811, Japan (e-mail: adachi.y+ieee@gmail.com).

Digital Object Identifier 10.1109/TIM.2023.3265750

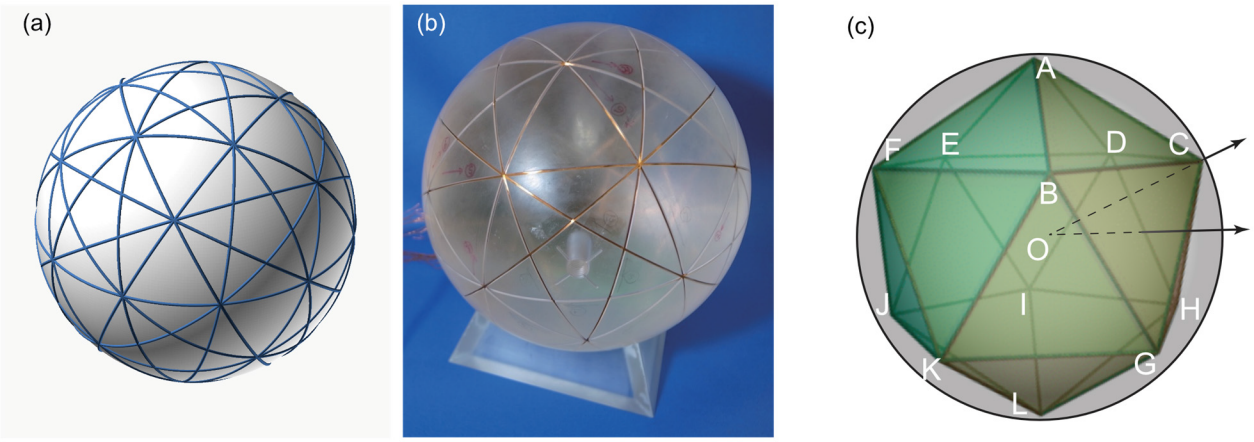

Fig. 1. (a) Conceptual design of the spherical coil array. (b) Actual appearance of the spherical coil array. (c) Regular icosahedron for determining the orientation of each concentric coil.

using the target field method to allow the application of a uniform reference magnetic field instead of Helmholtz coils. A method of calibration using a single coil to generate reference magnetic fields from multiple locations while changing the relative distance to the cryostat was also proposed [12]. However, while these methods would be effectively applied to the case that all sensors are oriented in the same direction such as a magnetocardiograph system, they are not suitable for the case that the sensors are oriented in various directions such as a whole-head MEG system. Another point of concern when using large calibration coils placed outside the cryostat is that the calibration may be affected by the distortion of the magnetic field distribution caused by the walls and floor of a narrow magnetically shielded room (MSR), which is made of high permeability materials.

In this study, we propose a novel coil array for the calibration of SQUID sensors of a whole-head MEG system. The shape of the proposed coil array was a single sphere that fits into the helmet-shaped sensor array. Multiple circular coils with a diameter of 150 mm are wound around the spherical coil bobbin. Moreover, we demonstrate that the structurally simple spherical coil array with large diameter coils allows for a more accurate calibration by the evaluation using a dry-type MEG phantom [13] than the one using our conventional calibration coil array composed of multiple three-axis coil bobbins [7], which is briefly described in Appendix A.

TABLE I
VERTICES OF AN ICOSAHEDRON

A	$(0, 0, 1)$	G	$(c, d, -a)$
B	$(2a, 0, a)$	H	$(-b, e, -a)$
C	(b, e, a)	I	$(-2a, 0, -a)$
D	$(-c, d, a)$	J	$(-b, -e, -a)$
E	$(-c, -d, a)$	K	$(c, -d, -a)$
F	$(b, -e, a)$	L	$(0, 0, -1)$

$$a = \frac{1}{\sqrt{5}}, b = \frac{1-a}{2}, c = \frac{1+a}{2}, d = \sqrt{b}, e = \sqrt{c}.$$

TABLE II
DIRECTIONAL VECTORS OF 16 COILS OF THE SPHERICAL CALIBRATION COIL ARRAY

(1)	(0, 0, 1)	(9)	(-0.6071, 0, 0.7947)
(2)	(0.8944, 0, 0.4472)	(10)	(-0.1876, 0.5774, 0.7947)
(3)	(0.2764, -0.8507, 0.4472)	(11)	(0.4911, 0.3568, 0.7947)
(4)	(-0.7236, -0.5257, 0.4472)	(12)	(0.7947, -0.5774, 0.1876)
(5)	(-0.7236, 0.5257, 0.4472)	(13)	(0.3035, -0.9342, -0.1876)
(6)	(0.2764, 0.8507, 0.4472)	(14)	(-0.3035, -0.9342, 0.1876)
(7)	(0.4911, -0.3568, 0.7947)	(15)	(-0.7947, -0.5774, -0.1876)
(8)	(-0.1876, -0.5774, 0.7947)	(16)	(-0.9822, 0, 0.1876)

II. MATERIALS AND METHODS

A. Design of the Spherical Coil Array

Fig. 1(a) and (b) illustrate the conceptual design and actual appearance of the newly proposed spherical coil array, respectively. It consists of 16 copper wire circular coils wound along grooves on the surface of an acrylic plastic sphere, as shown in Fig. 1(b). The diameter of the sphere was 152 mm. The widths and depths of the grooves were 1.0 mm. The sphere and grooves on its surface were precisely crafted using a numerically-controlled (NC) cutting machine with a tolerance of ±0.1 mm. Coils with a diameter of 150 mm were wound five turns and concentric to the sphere. The size of the sphere was determined to fit the helmet size of our MEG system for pediatric subjects [14], as well as the traditional whole-head MEG systems for adult subjects [15].

To evenly determine the orientation of each coil, a regular icosahedron concentric with the sphere, whose vertices A–L were parametrically defined, as shown in Fig. 1(c) and Table I, was assumed. Considering the symmetric property of an icosahedron, 16 coils were determined by directional vectors, as listed in Table II. Six coils, (1)–(6) in Table II, were oriented in the directions from the center of a sphere O to six vertexes of the icosahedron A–F, and the remaining 10 coils, (7)–(16) in Table II, were oriented to the centers of ten regular

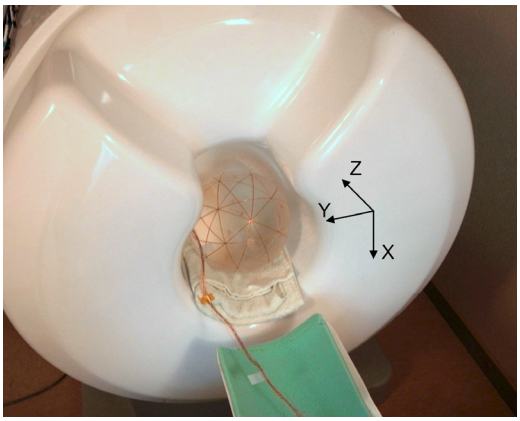

Fig. 2. Spherical coil array positioned in the MEG helmet.

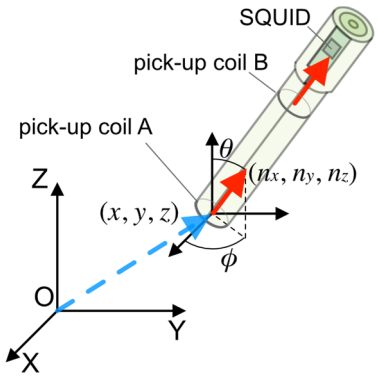

Fig. 3. Definition of the parameters for a sensor with an axial-type gradiometric pick-up coil. The blue dashed arrow and red arrow represent the position and orientation vectors, respectively.

triangles of the icosahedron faces, ΔABC, ΔACD, ΔADE, ΔAEF, ΔAFB, ΔBCG, ΔCGH, ΔCDH, ΔDHI, and ΔDEI. This set of coils is called a spherical coil array.

The 150-mm diameter of the proposed spherical calibration coil is much larger than those of the conventional calibration coil arrays, which are 5–60 mm [3], [4], [5], [6], [7]. The larger the diameter of the coil, the smaller the relative error of the coil shape from the design value even when it was machined with the same tolerance. A diameter of 150 mm is the maximal size that fits the helmets of various MEG systems, including those for pediatric subjects. Furthermore, it is expected that the structure of the spherical calibration coil will minimize assembly error. Conventional calibration coil arrays are assembled from multiple coil bobbins; therefore, assembly errors inevitably occur. However, the spherical calibration coil array bobbin is a single piece, and the fabrication error is determined only by the precision of the NC cutting machine. Consequently, the deviation between the parametrically represented coil used for the calculation of the theoretical reference magnetic fields and the realistically fabricated coil can be reduced, thereby allowing the accuracy of the calibration to be improved.

Regarding the number of coils, if it is not necessary to consider the uncertainty of the calibration, only six coils are sufficient for the calibration because, as described in Section II-B, the number of parameters needed to determine a single magnetometer is six, and theoretically, only six independent equations are required to estimate them. However, the number of coils must be increased to obtain reasonable calibration uncertainty, although the application of a large number of coils increases the time and effort required to fabricate the coil and measurements. In this study, in terms of the simplicity of the coil fabrication and symmetry of the coil arrangement, a bobbin shape based on the icosahedron was adopted, resulting in a set of 16 coils.

B. Calibration of a Whole-Head MEG System

Here, we demonstrate the calibration of a whole-head MEG system using a spherical coil array, applying it to the one developed and installed at Kanazawa Institute of Technology, which was composed of 160 axial-type SQUID gradiometers with a baseline length of 50 mm [15]. The MEG system was installed in an MSR in our laboratory and was originally calibrated using a conventional calibration coil array [7]. The spherical coil array was positioned in the helmet-shaped sensor array so that all SQUID sensors could capture the reference magnetic fields from the coils, as illustrated in Fig. 2. Each coil was excited by an 80-Hz sinusoidal tone burst current with an amplitude of 0.1 mA and a duration of 300 ms one after another to generate the reference magnetic field. The intensity of the detected reference magnetic fields was approximately 500–750 pT. The reference magnetic field signal from each coil was repeatedly recorded more than 64 times and averaged to improve the signal-to-noise ratio. After the recording, a fast Fourier transform (FFT) was applied to extract the 80-Hz component from the obtained data. Consequently, a set of 16 reference magnetic field signals, $\mathbf{V}_{\mathrm{meas}} = (V_{\mathrm{meas},1}, \ldots, V_{\mathrm{meas},16})$, from each coil was obtained for a single sensor.

The magnetic flux sensor in an MEG system is determined by the position $(x,\ y,\ z)$, orientation vector $(n_x,\ n_y,\ n_z)$, and sensitivity (g), as illustrated in Fig. 3. The determination of these parameters is called calibration. Here, the sensitivity indicates a coefficient to convert the obtained signal voltage from a sensor to the magnetic flux density, and its unit is T/V. Moreover, we introduced the polar coordinate system to represent the sensitivity orientation to simplify the numerical search as follows: the sensitivity orientation is indicated by two angles, θ and ϕ, instead of the orientation vector. In the case of axial-type gradiometers, which are widely applied in MEG systems, we assumed that the baseline orientation of the pick-up coil was identical to the sensitivity orientation.

Assuming that the center of the spherical coil array is positioned at the origin of the coordinate system, the theoretical value of the magnetic field from the jth circular coil $\mathbf{C}_j$ to be detected by a certain sensor (represented by $B_{\mathrm{cal},j}$) is calculated from i_j, the intensity of the current fed to $\mathbf{C}_j$, and the relative position of the sensor and $\mathbf{C}_j$. It is expressed as follows:

$$B_{\mathrm{cal},j} = F\left(\boldsymbol{\alpha}_{cj}, i_j \,|\, x, y, z, \theta, \phi\right) \tag{1}$$

where $\boldsymbol{\alpha}_{cj}$ represents the orientation of $\mathbf{C}_j$, as listed in Table II. In the case of circular coils, F represents a function including elliptic integrals [16]. When the sensor is a gradiometer, F includes subtraction of the magnetic field detected by a pick-up coil (pick-up coil B in Fig. 3) from the other (pick-up coil A). The six sensor parameters x, y, z, θ, ϕ, and g are obtained by numerical search based on a least-squares method to minimize L defined as

$$L = \Sigma_{j=1}^{16} |V_{\mathrm{cal},j} - V_{\mathrm{meas},j}|^2$$

where $V_{\mathrm{cal},j}$ represents the theoretical output voltage calculated from the theoretical magnetic field and sensitivity obtained by calibration. It is expressed as $V_{\mathrm{cal},j} = B_{\mathrm{cal},j}/g$, and $\mathbf{B}_{\mathrm{cal}} = (B_{\mathrm{cal},1}, \ldots, B_{\mathrm{cal},16})$ represents the set of theoretical magnetic fields from the 16 circular coils.

To simplify the numerical search and reduce the computational cost, we reduced the number of parameters to be searched to five, separating g from the numerical search, in accordance with the method described in Appendix B.

Instead of minimizing L, the five parameters of the sensor (x, y, z, θ, ϕ) should be selected to minimize the new evaluation value E determined as

$$E = 1 - \frac{(\mathbf{B}_{\mathrm{cal}} \cdot \mathbf{V}_{\mathrm{meas}})^2}{|\mathbf{B}_{\mathrm{cal}}|^2 |\mathbf{V}_{\mathrm{meas}}|^2}. \tag{2}$$

Parametric optimization based on the direct search method [17] was applied to determine the best set of five parameters. After the five optimal parameters were determined, g was determined as

$$g = \frac{|\mathbf{B}_{\mathrm{cal}}|^2}{\mathbf{B}_{\mathrm{cal}} \cdot \mathbf{V}_{\mathrm{meas}}}. \tag{3}$$

The obtained orientation angles (θ, ϕ) were converted into the orientation vector (n_x, n_y, n_z) as follows:

$$\begin{cases} n_x &= \sin\theta\cos\phi \\ n_y &= \sin\theta\sin\phi \\ n_z &= \cos\theta. \end{cases}$$

The volume inside the sphere was excluded from the region for the numerical search because there were no sensors in the sphere.

C. Estimation of Uncertainty in the Calibration

The results of the calibration described in Section II-B include uncertainties, which characterize the dispersion of the values and should be indicated for evaluating the reliability of values obtained by the calibration [18]. Here, we estimate the combined uncertainty in the calibration results from the error in the calibration measurement, which is represented by $\Delta V_j (= V_{\mathrm{cal},j} - V_{\mathrm{meas},j})$. Moreover, we investigated how $\Delta\mathbf{V} = (\Delta V_1, \Delta V_2, \ldots, \Delta V_{16})^T$ affects the fluctuations in the positions (Δx, Δy, Δz), orientations (Δn_x, Δn_y, Δn_z), and sensitivity (Δg) estimated in the calibration described in Section II-B. Notably, the number of independent parameters among n_x, n_y, and n_z is two, because $n_x^2 + n_y^2 + n_z^2 = 1$. Thus, the fluctuations in six sensor parameters $\Delta\mathbf{x} = (\Delta x, \Delta y, \Delta z, \Delta n_x, \Delta n_y, \Delta g)^T$ are discussed in the following paragraphs.

The relationship between $\Delta\mathbf{V}$ and $\Delta\mathbf{x}$ is expressed by the following equation using the first-order Taylor series approximation around the values obtained as the calibration result

$$\Delta\mathbf{V} = \mathbf{A}\Delta\mathbf{x} \tag{4}$$

where $\mathbf{A}$ represents a Jacobian matrix defined as

$$\mathbf{A} = \begin{pmatrix} \frac{\partial V_1}{\partial x} & \frac{\partial V_1}{\partial y} & \frac{\partial V_1}{\partial z} & \frac{\partial V_1}{\partial n_x} & \frac{\partial V_1}{\partial n_y} & \frac{\partial V_1}{\partial g} \\ \frac{\partial V_2}{\partial x} & \frac{\partial V_2}{\partial y} & \frac{\partial V_2}{\partial z} & \frac{\partial V_2}{\partial n_x} & \frac{\partial V_2}{\partial n_y} & \frac{\partial V_2}{\partial g} \\ \vdots & \vdots & \vdots & \vdots & \vdots & \vdots \\ \frac{\partial V_{16}}{\partial x} & \frac{\partial V_{16}}{\partial y} & \frac{\partial V_{16}}{\partial z} & \frac{\partial V_{16}}{\partial n_x} & \frac{\partial V_{16}}{\partial n_y} & \frac{\partial V_{16}}{\partial g} \end{pmatrix} \tag{5}$$

where V_j represents $V_{\mathrm{cal},j}$. To obtain $\Delta\mathbf{x}$ from $\Delta\mathbf{V}$, the transpose matrix of $\mathbf{A}$ is multiplied by both sides of (4), and $\mathbf{A}^T\Delta\mathbf{V} = \mathbf{A}^T\mathbf{A}\Delta\mathbf{x}$ was derived. $\mathbf{A}^T\mathbf{A}$ is a square matrix and its inverse matrix is calculated. Subsequently, $\Delta\mathbf{x}$ was obtained as follows:

$$\Delta\mathbf{x} = \left(\mathbf{A}^T\mathbf{A}\right)^{-1}\mathbf{A}^T\Delta\mathbf{V}. \tag{6}$$

The covariance matrix $\boldsymbol{\Sigma}$ was introduced to indicate the uncertainties in the estimated sensor parameters as variance values. This corresponds to $\Delta\mathbf{x}\Delta\mathbf{x}^T$ as follows:

$$\begin{aligned} \boldsymbol{\Sigma} &= \begin{pmatrix} \sigma_x^2 & \sigma_{xy}^2 & \sigma_{xz}^2 & \sigma_{xn_x}^2 & \sigma_{xn_y}^2 & \sigma_{xg}^2 \\ \sigma_{yx}^2 & \sigma_y^2 & \sigma_{yz}^2 & \sigma_{yn_x}^2 & \sigma_{yn_y}^2 & \sigma_{yg}^2 \\ \sigma_{zx}^2 & \sigma_{zy}^2 & \sigma_z^2 & \sigma_{zn_x}^2 & \sigma_{zn_y}^2 & \sigma_{zg}^2 \\ \sigma_{n_xx}^2 & \sigma_{n_xy}^2 & \sigma_{n_xz}^2 & \sigma_{n_x}^2 & \sigma_{n_xn_y}^2 & \sigma_{n_xg}^2 \\ \sigma_{n_yx}^2 & \sigma_{n_yy}^2 & \sigma_{n_yz}^2 & \sigma_{n_yn_x}^2 & \sigma_{n_y}^2 & \sigma_{n_yg}^2 \\ \sigma_{gx}^2 & \sigma_{gy}^2 & \sigma_{gz}^2 & \sigma_{gn_x}^2 & \sigma_{gn_y}^2 & \sigma_g^2 \end{pmatrix} \\ &= \begin{pmatrix} \Delta x\Delta x & \Delta x\Delta y & \cdots & \Delta x\Delta g \\ \Delta y\Delta x & \Delta y\Delta y & \cdots & \Delta y\Delta g \\ \vdots & \vdots & \ddots & \vdots \\ \Delta g\Delta x & \Delta g\Delta y & \cdots & \Delta g\Delta g \end{pmatrix} = \Delta\mathbf{x}\Delta\mathbf{x}^T \end{aligned} \tag{7}$$

where σ_x, σ_y, σ_z, σ_{nx}, σ_{ny}, and σ_g correspond to the uncertainties of x, y, z, n_x, n_y, and g, respectively. Using (6), (7) is deformed to

$$\begin{aligned} \boldsymbol{\Sigma} = \Delta\mathbf{x}\Delta\mathbf{x}^T &= \left(\mathbf{A}^T\mathbf{A}\right)^{-1}\mathbf{A}^T\Delta\mathbf{V}\left(\left(\mathbf{A}^T\mathbf{A}\right)^{-1}\mathbf{A}^T\Delta\mathbf{V}\right)^T \\ &= \left(\mathbf{A}^T\mathbf{A}\right)^{-1}\mathbf{A}^T\Delta\mathbf{V}\Delta\mathbf{V}^T\mathbf{A}\left(\left(\mathbf{A}^T\mathbf{A}\right)^{-1}\right)^T \\ &= \left(\mathbf{A}^T\mathbf{A}\right)^{-1}\mathbf{A}^T\Delta\mathbf{V}\Delta\mathbf{V}^T\mathbf{A}\left(\mathbf{A}^T\mathbf{A}\right)^{-1} \end{aligned} \tag{8}$$

where

$$\Delta\mathbf{V}\Delta\mathbf{V}^T = \begin{pmatrix} \Delta V_1\Delta V_1 & \Delta V_1\Delta V_2 & \cdots & \Delta V_1\Delta V_{16} \\ \Delta V_2\Delta V_1 & \Delta V_2\Delta V_2 & \cdots & \Delta V_2\Delta V_{16} \\ \vdots & \vdots & \ddots & \vdots \\ \Delta V_{16}\Delta V_1 & \Delta V_{16}\Delta V_2 & \cdots & \Delta V_{16}\Delta V_{16} \end{pmatrix}.$$

Assuming $\Delta V_i \Delta V_j \rightarrow 0 (i \neq j)$ and $\Delta V_i \Delta V_j \rightarrow \sigma^2 (i = j)$, $\Delta\mathbf{V}\Delta\mathbf{V}^T \rightarrow \sigma^2\mathbf{I}$ is obtained, where $\mathbf{I}$ is a 16×16 unit matrix. The variance value σ^2 can be inferred from the difference between the theoretical reference magnetic field signals and the measured magnetic field signals as

$$\hat{\sigma}^2 = \frac{\sum_{j=1}^{16} \Delta V_j^2}{16-1} = \frac{\sum_{j=1}^{16} \left(V_{\mathrm{cal},j} - V_{\mathrm{meas},j}\right)^2}{15}. \quad (9)$$

Consequently, the covariance matrix $\mathbf{\Sigma}$ was calculated using (8) as follows:

$$\mathbf{\Sigma} = \left(\mathbf{A}^T\mathbf{A}\right)^{-1}\mathbf{A}^T\hat{\sigma}^2\mathbf{I}\mathbf{A}\left(\mathbf{A}^T\mathbf{A}\right)^{-1} = \hat{\sigma}^2\left(\mathbf{A}^T\mathbf{A}\right)^{-1}. \quad (10)$$

The uncertainty in n_z is estimated by the error propagation law as follows:

$$\sigma_{n_z}^2 = \left(\frac{\partial n_z}{\partial n_x}\right)^2 \sigma_{n_x}^2 + \left(\frac{\partial n_z}{\partial n_y}\right)^2 \sigma_{n_y}^2. \quad (11)$$

Using (10) and (11), we estimate the combined uncertainty in the calibration described in Section II-B.

D. Evaluation of Accuracy Using the Dry-Type MEG Phantom

A dry-type MEG phantom was used to evaluate the calibration results. The dry-type MEG phantom emulated MEG signals using long isosceles triangle coils, based on Ilmoniemi's model [19]. In total, 50 triangular coils with a base and height of 5 and 65 mm, respectively, were arranged in quasi-spherical symmetry, so that their apexes were at the center of the sphere. The base of each triangular coil corresponds to an equivalent current dipole (ECD), and the magnetic field distribution generated from each triangular coil approximately follows Sarvas' equation for a spherical conductor [20]. The position of each triangular coil of the dry-type MEG phantom used in this study was precisely measured using an X-ray CT machine and a coordinate-measuring machine. An effective ECD was defined based on the position and orientation of the corresponding calibrated triangular coil and was regarded as the ground truth of the ECDs. The measurement method and values of the parameters of all effective ECDs were reported in [13]. The uncertainty in the position of the effective ECDs was ± 0.1 mm.

A dry-type MEG phantom was set in the helmet of the calibrated MEG system. One of the 50 triangular coils accidentally broke during the experiment. Therefore, the remaining 49 triangular coils were sequentially excited by an 11-Hz sinusoidal current with an intensity of 0.01 mA and a duration of 181.8 ms one after another, and the distribution of the generated magnetic signals was captured by the MEG system. The position and orientation of the dry-type MEG phantom relative to the sensor array were determined using marker coil localization, as in our previous studies [7], [13]. ECD localization based on the moving dipole model, which is a conventional magnetic source analysis for MEG [1], was applied to the magnetic field signals generated from each triangular coil, and 49 estimated ECDs were obtained. The differences in the positions, orientations, and intensities of the effective and estimated ECDs were determined to evaluate the validity of the calibration.

III. Results

A. Calibration Results With Uncertainties

Fig. 4 illustrates isofield contour maps indicating the distributions of the reference magnetic fields captured by the MEG sensor array generated from each of the 16 coils. Each sensor in the array detects the reference magnetic fields from the coils at sufficient intensity. To clearly indicate the magnetic field signals from the first coil, only the first coil was intentionally wound in three turns, not five. Consequently, the intensity of the magnetic field from the first coil was made smaller than those from the other coils wound five turns.

The calibration procedure was applied to the magnetic field data obtained from the spherical calibration coil array, and a set of five parameters, x, y, z, θ, ϕ, and the sensitivity g, were estimated for each sensor. Fig. 5 illustrates the results of the calibration and calculation of the uncertainty. A 3-D plot of Fig. 5(a) reveals that both the position and orientation were appropriately estimated. Meanwhile, the sensitivity was estimated as 1.13 ± 0.05 nT/V on average (mean $\pm$ standard deviation (SD) of 160 sensors). The maximum uncertainty in the sensitivity was estimated to be ± 0.023 nT/V. The goodness of fit (GOF) of each sensor was calculated using the following formula:

$$\mathrm{GOF} = \left(1 - \frac{\sum_{j=1}^{16} \left(B_{\mathrm{cal},j} - g V_{\mathrm{meas},j}\right)^2}{\sum_{j=1}^{16} \left(g V_{\mathrm{meas},j}\right)^2}\right) \times 100(\%). \quad (12)$$

Accordingly, it was determined as $99.9998\% \pm 0.0002\%$ on average (mean $\pm$ SD of 160 sensors). The worst GOF was 99.9989%. This indicated that the estimation of the parameters was successfully executed for each sensor. Five sensors at typical positions marked in red in Fig. 5(b) and (c) in the parietal, frontal, occipital, and temporal areas were selected, and their parameters are summarized with the uncertainties in Table III.

B. Evaluation of Accuracy Using the Dry-Type MEG Phantom

It is difficult to evaluate the validity of the calibration by comparing the estimated sensor parameters directly to their designed values because the positions of the sensors shift unpredictably from the designed values due to the cryogenic temperature. Instead, the validity of the calibration was assessed by evaluating the source localization accuracy using the dry-type MEG phantom described in Section II-D. The displacements between the effective and estimated positions,

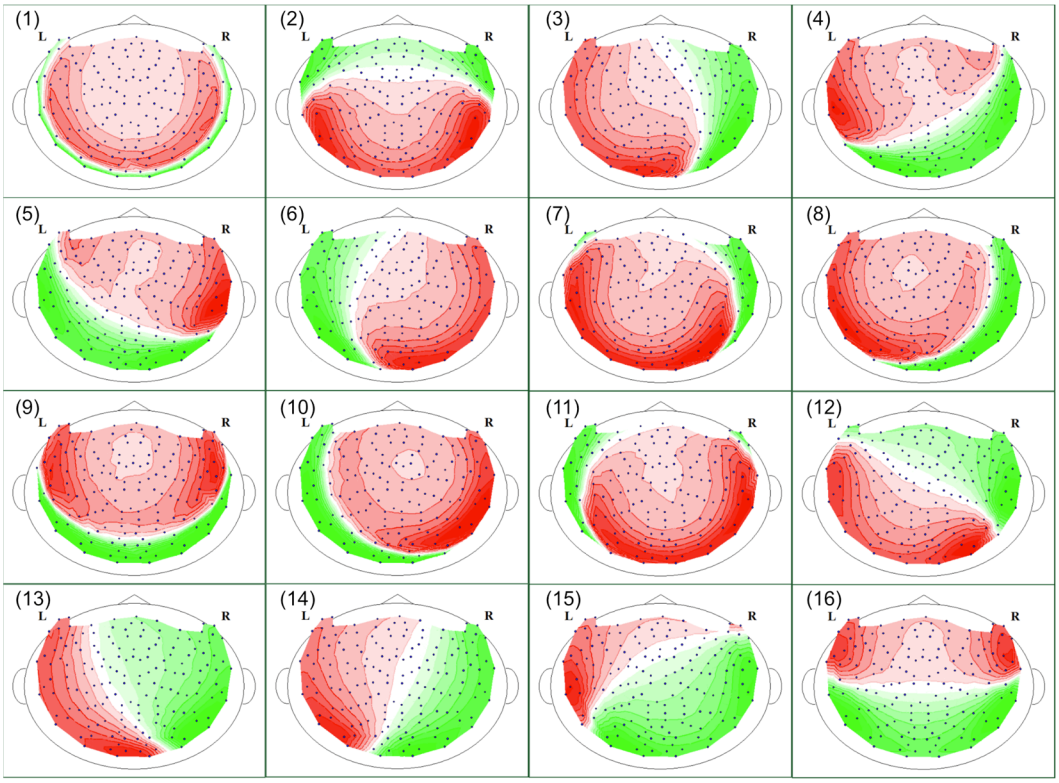

Fig. 4. Sixteen distribution patterns of the reference magnetic fields. The red and green areas indicate opposite magnetic field orientations from each other. A step between contours corresponds to 75 pT. The labels (1)–(16) correspond to those in Table II.

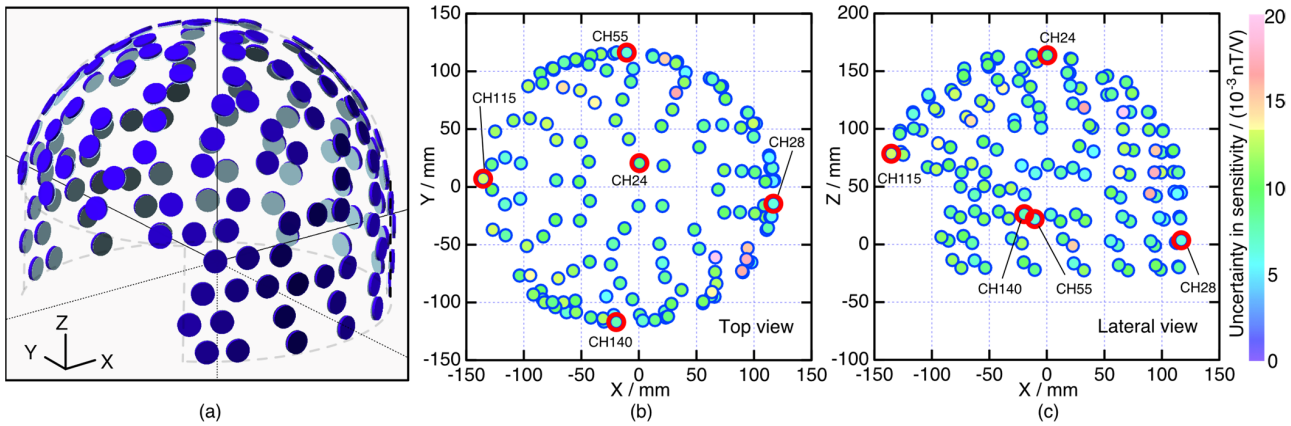

Fig. 5. Results of the calibration of the 160 sensors. (a) Three-dimensional plot indicating the estimated sensor position and orientation. (b) and (c) Position of sensors projected on *XY* and *XZ* planes, respectively. The marker color represents uncertainty in sensitivity.

TABLE III
SENSOR PARAMETERS WITH UNCERTAINTIES

channel	x (mm)	y (mm)	z (mm)	n_x	n_y	n_z	g (nT/V)
CH24	0.39±0.47	20.72±0.46	163.84±0.33	0.1028±0.0069	0.1757±0.0066	0.9791±0.0014	1.176±0.009
CH28	116.76±0.18	-14.51±0.24	3.61±0.19	0.9929±0.0007	-0.1178±0.0056	0.0157±0.0009	1.135±0.006
CH55	-10.63±0.27	116.38±0.17	22.02±0.36	0.0262±0.0064	0.9993±0.0002	-0.0254±0.0003	1.065±0.007
CH115	-135.52±0.47	7.07±0.50	78.59±0.49	-0.2907±0.0022	0.3784±0.0079	0.8788±0.0022	1.137±0.013
CH140	-19.74±0.34	-116.89±0.26	26.20±0.46	-0.0926±0.0077	-0.9951±0.0009	0.0352±0.0011	1.038±0.008

The values following the plus-minus signs (±) correspond to uncertainties with a coverage factor k=1.

orientations, and intensities of each ECD are estimated, and their means and standard errors are presented in Fig. 6. The results from our previous study for the calibration of the MEG system with a conventional coil array composed of

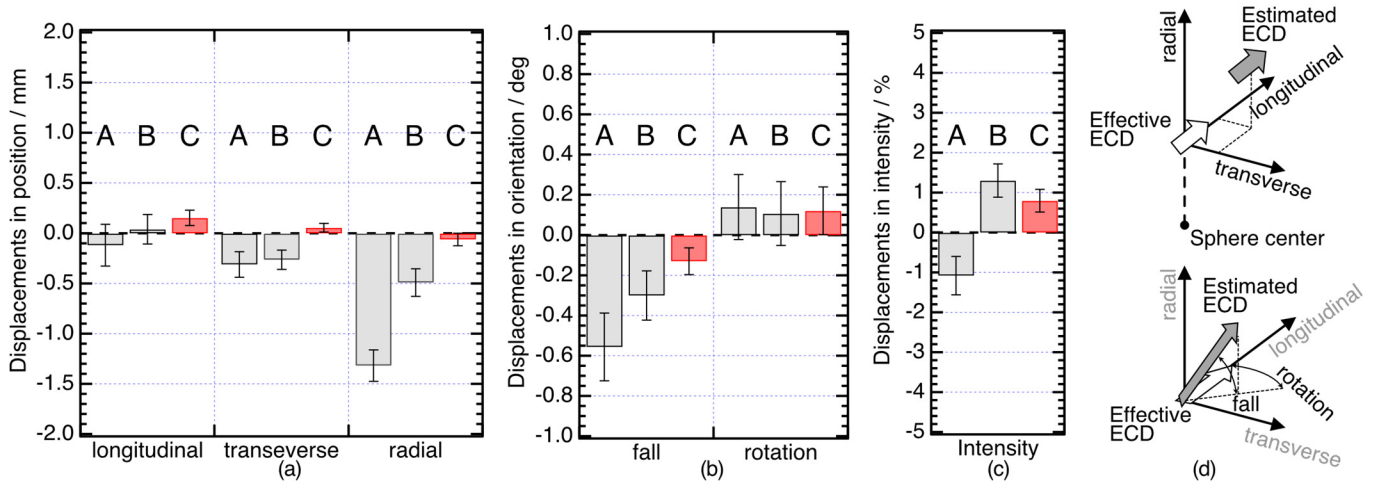

Fig. 6. Mean displacements and the standard errors between the effective and estimated ECDs in terms of (a) position, (b) orientation, and (c) intensity. Here, A–C correspond to the results from the conventional coil array with designed values, from the conventional coil array whose coil geometry was measured using X-ray CT, and from the spherical coil array, respectively. (d) Definition of the displacements in position (upper) and orientation (lower) between the effective and estimated ECDs. The values for A and B were excerpted from [7].

multiple three-axis coil bobbins are also presented in Fig. 6 for comparison.

IV. Discussions

The positions and orientations of the SQUID gradiometers indicated in Fig. 5 and Table III are described in the coordinate system determined by the center position and orientation of the spherical calibration coil array. Therefore, the values can be slightly different each time it is calibrated, because it is difficult to place the coil array in a perfectly identical position and orientation in the helmet. However, the absolute sensor positions in a particular coordinate system are not essential because, when the MEG is applied to actual subjects and magnetic source analysis is performed, the sensor geometry in the coordinate system determined in the calibration process is transformed to the coordinate system with regard to the head of the subject, that is, the head coordinate system. This transformation is called "co-registration" in general and is performed using rigid body transformation that includes rotations and translations of the entire coordinate system, as described in detail in [21].

The MEG sensor array calibrated in this study was identical to that described in our previous study, with a conventional calibration coil array composed of multiple three-axis coil bobbins [7]. The values for the positions and orientations of each sensor were obtained in the coordinate system with respect to the conventional calibration coil array, in which the orientation of the helmet was inverted axisymmetrically around the z-axis with respect to the orientation shown in Fig. 5. However, the values can be transformed to the dry-type MEG phantom coordinate system by co-registration, as well as those based on the spherical calibration coil array when the phantom verification described in Section II-D is performed.

As indicated by (10), the uncertainty is expressed as a product of $\hat{\sigma}^2$, which corresponds to the difference between the theoretical reference magnetic field signals and the measured magnetic field signals, and $(\mathbf{A}^T\mathbf{A})^{-1}$, which corresponds to an inverse of the sum of squares and cross product matrix of the Jacobian matrix $\mathbf{A}$. $\hat{\sigma}^2$ depends on various factors, such as the error in the fabrication of the spherical coils, temperature variation in the laboratory, intrinsic noise of the magnetometers, fluctuation of the residual background magnetic fields in the MSR, distortion in the distribution of the reference magnetic fields caused by the eddy current in the metallic parts, the existence of magnetic materials near the measurement area, error in the algorithm for numerical search, incompatibility of the parametric model of the sensor, etc. Accordingly, the uncertainties discussed in this study include those originating from the causes described above. Therefore, even though a set of the MEG system and the calibration coil array was identical, calibration under different conditions would result in different uncertainty. In contrast, the Jacobian matrix is determined only by the structure of the coil array, the current applied to the coils, and the relative positions between the magnetometer and coils. Therefore, the consideration of $\mathbf{A}^T\mathbf{A}$ allows us to evaluate the coil array design itself, eliminating other factors, such as the influence of measurement conditions and fabrication accuracy. When we assumed that the conventional coil array was applied to the calibration described in Section II-B, the $\mathbf{A}^T\mathbf{A}$ elements were all calculated to be smaller than those calculated using the spherical coil array, and most of them were smaller by at least a factor of ten. This indicates that the spherical coil array structurally provides smaller uncertainties when $\hat{\sigma}^2$ is comparable for both coil arrays.

As indicated in Fig. 6, the difference between the effective and estimated positions of the ECDs obtained from the phantom verification was less than 0.2 mm on average. When the MEG from actual human subjects is measured, the combined uncertainty of the MEG measurement includes the uncertainties from the subject positioning and the uncertainties from the co-registration between the MEG and the anatomical information from magnetic resonance imaging, which are often on the order of millimeters or even centimeters. Therefore, the displacement between the effective and estimated

ECDs obtained during the phantom verification should be acceptable.

In our previous study, we discussed the improvements in sensor array calibration using a conventional coil array composed of multiple three-axis coil bobbins. Compared with the results from the sensor array calibrated by the conventional coil array with the designed values (A), the source localization accuracy was enhanced when the coil geometry was precisely measured using X-ray CT (B) [7]. In this study, even though the geometry of the spherical calibration coil array was not measured by X-ray CT, comparable or smaller deviations between the effective and estimated ECDs were obtained (C), indicating that calibration with the spherical coil array could provide higher accuracy than that with the conventional coil array. The reasons for the higher accuracy are attributable to the relatively small mechanical error of the large diameter of the coils and the fact that the assembly error was small because all coils were wound on a single precisely machined spherical bobbin. Accordingly, the spherical calibration coil array is readily fabricated at the same level of accuracy as the conventional coil array composed of multiple three-axis coil bobbins whose geometry is precisely measured by X-ray CT. This is another advantage of the spherical calibration coil array, as it is important for the calibration coil arrays to be reproduced easily and shorten the calibration process.

For parametric optimization to determine the positions and orientations of the sensors, the initial values for each parameter must be provided at the beginning of the numerical search. Determining the initial values was critical for obtaining valid calibration results using the spherical coil array, primarily because the sensor position was occasionally estimated at the opposite spherically symmetric side owing to the perfect symmetry of the coil geometry. If the designed values for each parameter are available, limiting the range of the numerical search to the vicinity of the designed values will allow the search to converge efficiently and avoid inappropriate results owing to local minima. Furthermore, one or two non-centric coils should be added to the coil array to break the symmetry when designing the next version of the spherical calibration coil array.

As shown in Fig. 3, the SQUID sensors were modeled with a single sensitivity point at the center of the pick-up coil for both the calibration and phantom analyses, assuming a uniform magnetic field in the pick-up coil. However, the diameter of the pick-up coil was 15.5 mm, and the magnetic field in the pick-up coil could not be considered uniform. In this study, we indicated an improvement in the accuracy of the phantom test results compared to that of the results obtained with the conventional calibration coil array under the same condition as that for the single sensitivity point model used in previous studies. When we consider the non-uniformity of the reference magnetic fields in the pick-up coils in our future study, it is expected that the accuracy of the calibration and phantom results will be further improved.

In this study, the sensor array to be calibrated was a SQUID-based whole-head MEG. Calibration using coil arrays after cooling is essential because of the unpredictable distortion of the plastic parts at cryogenic temperatures and the opacity of the cryostat, preventing the measurement of the sensor position and orientation from the outside. In the case of SQUID-based MEG systems, calibration is performed once after installation and is usually not required afterward because the SQUID sensors are preserved in liquid helium at the constant temperature of 4.2 K and their position, orientation, and sensitivity are quite stable as long as they are kept at such a super-low temperature.

In contrast to SQUID sensors, sensor arrays of "on-scalp" MEG systems that use non-cryogenic magnetic flux sensors, such as optically pumped magnetometers (OPMs) [22], [23], [24], [25] or magnetoresistive (MR) sensors [26], [27], have recently gained increasing attention. Importantly, the sensor arrays of on-scalp MEG systems have small distortions because they are not exposed to extremely low temperatures. Moreover, the position of each sensor can be measured from the outside using 3-D digitization techniques because there is no opacity cryostat. However, the calibration proposed in this study will still be effective to exploit the on-scalp MEG systems, which have the adjustability of sensor positions. Accordingly, the position of each sensor can be adjusted to fit the shape of each subject's head. The calibration that we propose can provide a mean for revealing the positions, orientations, and sensitivities of multiple sensors for a short time after adjusting the sensor positions. In the case of on-scalp MEG systems, the sensor positions are closer to the magnetic sources than those of conventional SQUID-based MEGs. Magnetic fields closer to the sources have a steeper gradient. Therefore, even small uncertainties in the calibration can significantly affect the accuracy of source localization. Consequently, a more accurate calibration is required for on-scalp MEG systems, and the importance of a spherical coil array with a larger diameter in calibration is expected to be significant.

V. Conclusion

In this study, we proposed a spherical coil array for the calibration of a whole-head MEG sensor array. The results of the source localization experiment using the dry-type MEG phantom indicated that the spherical coil array was effective in improving the accuracy of the calibration compared with the conventional coil array composed of multiple three-axis coil bobbins. It was also demonstrated that the uncertainties in the calibration could be estimated for each sensor based on the difference between the theoretical reference magnetic field signals and the actual captured magnetic field signals. The identification of uncertainties helps MEG users to quantitatively understand the reliability of calibration results. It can also be used as an index in the design of new and improved calibration coil arrays in the future.

Appendix

A. Calibration Coil Array Composed of Multiple Three-Axis Coil Bobbins

In this study, we evaluated the result of the calibration using a spherical coil array. The phantom test revealed that the calibration using the spherical coil array provided more

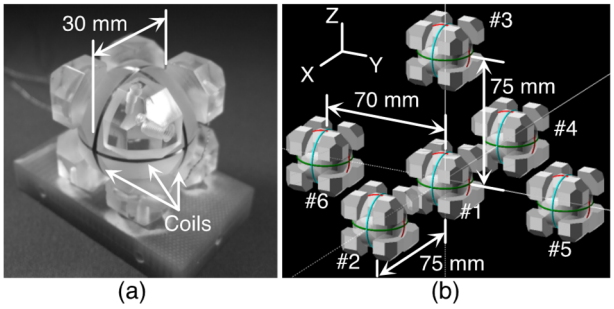

Fig. 7. (a) Bobbin for three orthogonal circular coils. (b) Arrangement of the bobbins. All values are the designed ones.

accurate source localization results than those obtained with a conventional calibration coil array composed of multiple three-axis coil bobbins. The structure of the conventional calibration coil array is briefly described here as an appendix. The details of the conventional coil array and the measurement of its geometry using X-ray CT are described in [7].

Fig. 7 shows a three-axis coil bobbin and the configuration of the entire coil array. Three 30-mm diameter circular coils were orthogonally combined into a bobbin precisely machined from an acrylic plastic block as shown in Fig. 7(a). Six bobbins were three-dimensionally arranged as shown in Fig. 7(b) and fixed to a plastic support. In total, the coil array comprised 18 coils. The number of turns in each coil was ten.

The calibration procedures were the same as those described in Section II-B. A set of 18 coils combined was inserted into the helmet-shaped sensor array of a whole-head MEG such that coil 3 was in close proximity to the top of the helmet.

The geometry of the conventional calibration coil array described above was precisely measured using an X-ray CT machine. The differences between the designed values and those measured by the X-ray CT were 0.6 ± 0.3 mm, 0.7°± 0.4°, and 0.3 ± 0.3 mm (mean ± SD of 160 sensors) with respect to the center position, orientation, and radius, respectively. The result of the phantom test indicated that the source localization accuracy of the MEG system could be improved by the calibration using a three-dimensional measured coil array geometry rather than by using the designed values, as shown in Fig. 6.

B. Evaluation Value for the Calibration Process

In the calibration process, each magnetometer was determined by a set of six parameters: position (x, y, z), orientation (θ, ϕ), and sensitivity (g), as described in Section II-B. These six parameters were obtained by a numerical search based on a least-squares method to minimize L, defined as

$$L = \Sigma_{j=1}^{16} |V_{\mathrm{cal},j} - V_{\mathrm{meas},j}|^2.$$

When $V_{\mathrm{cal},j} = sB_{\mathrm{cal},j}$, where $s = 1/g$, L is transformed as follows:

$$\begin{aligned} L &= \Sigma_{j=1}^{16} |s B_{\mathrm{cal},j} - V_{\mathrm{meas},j}|^2 \\ &= s^2 |\mathbf{B}_{\mathrm{cal}}|^2 - 2s\mathbf{B}_{\mathrm{cal}}\cdot\mathbf{V}_{\mathrm{meas}} + |\mathbf{V}_{\mathrm{meas}}|^2. \end{aligned} \tag{A1}$$

Because $\mathbf{B}_{\mathrm{cal}}$ does not contain s, s was obtained separately. When L is minimized, the partial derivative of s becomes zero ($\partial L/\partial s = 0$). Therefore, from (A1), the following equation holds:

$$2\, s|\mathbf{B}_{\mathrm{cal}}|^2 - 2\mathbf{B}_{\mathrm{cal}}\cdot\mathbf{V}_{\mathrm{meas}} = 0.$$

Then, s is obtained as

$$s = \frac{\mathbf{B}_{\mathrm{cal}}\cdot\mathbf{V}_{\mathrm{meas}}}{|\mathbf{B}_{\mathrm{cal}}|^2}. \tag{A2}$$

Substituting (A2) into (A1), we obtain

$$L = -\frac{(\mathbf{B}_{\mathrm{cal}}\cdot\mathbf{V}_{\mathrm{meas}})^2}{|\mathbf{B}_{\mathrm{cal}}|^2} + |\mathbf{V}_{\mathrm{meas}}|^2. \tag{A3}$$

Dividing both sides of (A3) by $|\mathbf{V}_{\mathrm{meas}}|^2$, we obtain

$$\frac{L}{|\mathbf{V}_{\mathrm{meas}}|^2} = 1 - \frac{(\mathbf{B}_{\mathrm{cal}}\cdot\mathbf{V}_{\mathrm{meas}})^2}{|\mathbf{B}_{\mathrm{cal}}|^2|\mathbf{V}_{\mathrm{meas}}|^2}.$$

Replacing the left-hand side with E yields (2).

As $|\mathbf{V}_{\mathrm{meas}}|^2$ is a constant for the numerical search, we can perform a numerical search to minimize E to obtain the optimal set of five parameters (x, y, z, θ, and ϕ) instead of minimizing L. The second right-hand term corresponds to the square of the cosine similarity between $\mathbf{B}_{\mathrm{cal}}$ and $\mathbf{V}_{\mathrm{meas}}$. This implies that E is minimized when the similarity in the signal space between $\mathbf{V}_{\mathrm{cal}}$ ($=\mathbf{B}_{\mathrm{cal}}/g$) and $\mathbf{V}_{\mathrm{meas}}$ is the highest. In this way, by separating g from the numerical search, we can reduce the number of parameters to be searched from six to five and shorten the computation time. After the five optimal parameters are obtained, g is determined as

$$\begin{aligned} g &= 1/s \\ &= \frac{|\mathbf{B}_{\mathrm{cal}}|^2}{\mathbf{B}_{\mathrm{cal}}\cdot\mathbf{V}_{\mathrm{meas}}} \end{aligned}$$

which is the same as (3) in Section II-B.

ACKNOWLEDGMENT

The authors thank Yoko Oshida for her artistic wiring works to fabricate the spherical calibration coil array. They also thank Editage (www.editage.jp) for the English language editing.

REFERENCES

[1] M. Hämäläinen, R. Hari, R. J. Ilmoniemi, J. Knuutila, and O. V. Lounasmaa, "Magnetoencephalography—Theory, instrumentation, and applications to noninvasive studies of the working human brain," *Rev. Modern Phys.*, vol. 65, no. 2, pp. 413–497, Apr. 1993, doi: 10.1103/RevModPhys.65.413.

[2] M. Kawakatsu et al., "A calibration of the sensitivity and position of the sensors for whole-head vector SQUID magnetoencephalography system and positioning for the system," *J. Jpn. Biomagn. Bioelectromagn. Soc.*, vol. 12, no. 2, pp. 3–9, 1999.

[3] T. Yoshida, M. Higuchi, T. Komuro, and H. Kado, "Calibration system for a multichannel squid magnetometer," in *Proc. 16th Annu. Int. Conf. IEEE Eng. Med. Biol. Soc.*, Nov. 1994, pp. 171–172.

[4] A. Pasquarelli et al., "Calibration of a vector-meg helmet system," *Neurol. Clin. Neurophysiol.*, vol. 94, Nov. 2004, Art. no. 16012682.

[5] Y. Adachi, M. Higuchi, D. Oyama, Y. Haruta, S. Kawabata, and G. Uehara, "Calibration for a multichannel magnetic sensor array of a magnetospinography system," *IEEE Trans. Magn.*, vol. 50, no. 11, pp. 1–4, Nov. 2014, doi: 10.1109/TMAG.2014.2326869.

[6] V. Vivaldi, S. Sommariva, and A. Sorrentino, "A simplex method for the calibration of a MEG device," *Commun. Appl. Ind. Math.*, vol. 10, no. 2, pp. 35–46, Jan. 2019, doi: 10.2478/caim-2019-0005.

[7] D. Oyama, Y. Adachi, M. Higuchi, and G. Uehara, "Calibration of a coil array geometry using an X-ray computed tomography," *IEEE Trans. Magn.*, vol. 58, no. 2, pp. 1–5, Feb. 2022, doi: 10.1109/TMAG.2021.3080673.

[8] S. G. Lee, C. S. Kang, and J. W. Chang, "Square loop coil system for balancing and calibration of second-order squid gradiometers," *IEEE Trans. Appl. Supercond.*, vol. 17, no. 2, pp. 3769–3772, Jun. 2007, doi: 10.1109/TASC.2007.898868.

[9] T. Beravs, S. Begus, J. Podobnik, and M. Munih, "Magnetometer calibration using Kalman filter covariance matrix for online estimation of magnetic field orientation," *IEEE Trans. Instrum. Meas.*, vol. 63, no. 8, pp. 2013–2020, Aug. 2014, doi: 10.1109/TIM.2014.2302240.

[10] H. Li, S.-L. Zhang, C.-X. Zhang, X.-Y. Kong, and X.-M. Xie, "An efficient calibration method for SQUID measurement system using three orthogonal Helmholtz coils," *Chin. Phys. B*, vol. 25, no. 6, 2016, Art. no. 16012682, doi: 10.1088/1674-1056/25/6/068501.

[11] K. Yang et al., "Calibration of SQUID magnetometers in multichannel MCG system based on bi-planar coil," *IEEE Trans. Instrum. Meas.*, vol. 71, pp. 1–9, 2022.

[12] A. C. Bruno and P. C. Ribeiro, "Spatial Fourier calibration method for multichannel SQUID magnetometers," *Rev. Sci. Instrum.*, vol. 62, no. 4, pp. 1005–1009, Apr. 1991, doi: 10.1063/1.1142049.

[13] D. Oyama, Y. Adachi, M. Yumoto, I. Hashimoto, and G. Uehara, "Dry phantom for magnetoencephalography—Configuration, calibration, and contribution," *J. Neurosci. Methods*, vol. 251, pp. 24–26, Aug. 2015, doi: 10.1016/j.jneumeth.2015.05.004.

[14] Y. Adachi et al., "Development of a whole-head child MEG system," in *Proc. 17th Int. Conf. Biomagnetism Adv. Biomagnetism*, S. Supek and A. Susac, Eds. Berlin, Germany: Springer, 2010, pp. 35–38, doi: 10.1007/978-3-642-12197-5_3.

[15] H. Kado et al., "Magnetoencephalogram systems developed at KIT," *IEEE Trans. Appl. Supercond.*, vol. 9, no. 2, pp. 4057–4062, Jun. 1999, doi: 10.1109/77.783918.

[16] L. D. Landau, E. M. Lifshitz, and L. P. Pitaevskii, *Landau and Lifshitz Course of Theoretical Physics*, vol. 8. Izmir Province, Turkey: Pergamon, 1984.

[17] R. Hooke and T. A. Jeeves, "'Direct search' solution of numerical and statistical problems," *J. ACM*, vol. 8, no. 2, pp. 212–229, Apr. 1961.

[18] *BIPM, IEC, IFCC, ILAC, ISO, IUPAC, IUPAP, and OIML, Evaluation of Measurement Data—Guide to the Expression of Uncertainty in Measurement*, Joint Committee Guides Metrol. (JCGM), Bureau International des Poids et Mesures (BIPM), France, 2008. [Online]. Available: https://www.bipm.org

[19] R. J. Ilmoniemi, M. S. Hämäläinen, and J. Knuutila, "The forward and inverse problem in the spherical model," in *Biomagnetism: Applications and Theory*, New York, NY, USA: Pergamon, 1985, pp. 82–278.

[20] J. Sarvas, "Basic mathematical and electromagnetic concepts of the biomagnetic inverse problem," *Phys. Med. Biol.*, vol. 32, no. 1, pp. 11–22, 1987.

[21] J. H. Challis, "A procedure for determining rigid body transformation parameters," *J. Biomech.*, vol. 28, no. 6, pp. 733–737, 1995.

[22] A. Borna et al., "A 20-channel magnetoencephalography system based on optically pumped magnetometers," *Phys. Med. Biol.*, vol. 62, no. 23, pp. 8909–8923, 2017, doi: 10.1088/1361-6560/aa93d1.

[23] E. Boto et al., "Moving magnetoencephalography towards real-world applications with a wearable system," *Nature*, vol. 555, no. 7698, pp. 657–661, Mar. 2018, doi: 10.1038/nature26147.

[24] J. F. Schneiderman, S. Ruffieux, C. Pfeiffer, and B. Riaz, "On-scalp MEG," in *Magnetoencephalography*, S. Spek and C. Aine, Eds. Cham, Switzerland: Springer, 2019, pp. 1313–1335.

[25] R. M. Hill et al., "Multi-channel whole-head OPM-MEG: Helmet design and a comparison with a conventional system," *NeuroImage*, vol. 219, Oct. 2020, Art. no. 116995, doi: 10.1016/j.neuroimage.2020.116995.

[26] A. Kanno et al., "Scalp attached tangential magnetoencephalography using tunnel magneto-resistive sensors," *Sci. Rep.*, vol. 12, no. 1, p. 6106, Apr. 2022, doi: 10.1038/s41598-022-10155-6.

[27] Y. Adachi, S. Kawabata, T. Tatsuoka, and Y. Terazono, "Emerging MR sensors for biomagnetic measurements," in *Flexible High Performance Magnetic Field Sensors*, E. Labyt, T. Sander, and R. Wakai, Eds. Cham, Switzerland: Springer, 2022, pp. 299–312.

Yoshiaki Adachi (Member, IEEE) received the M.E. and Ph.D. degrees from Osaka University, Osaka, Japan, in 1994 and 2007, respectively.

He worked in the field of MEG measurement at the Electrotechnical Laboratory, MITI, Ibaraki, Japan, from 1994 to 1997. He has been working in research and development of the SQUID and other magnetic flux sensors, their applications, and signal processing at the Applied Electronics Laboratory, Kanazawa Institute of Technology, Ishikawa, Japan, since 1998. In 2015, he became a Professor at the Kanazawa Institute of Technology.

Dr. Adachi is a member of the Institute of Electrical Engineering of Japan, the Magnetics Society of Japan, and the Japan Biomagnetism and Bioelectromagnetics Society.

Daisuke Oyama (Member, IEEE) was born in Miyagi, Japan. He received the M.E. and Dr.Eng. degrees in engineering from Iwate University, Morioka, Japan, in 2006 and 2009, respectively.

Since 2009, he has been with the Applied Electronics Laboratory, Kanazawa Institute of Technology, Ishikawa, Japan, where he is currently an Associate Professor. His current research interests include magnetic sensors, biomagnetic measurements, and magnetic resonance imaging (MRI).

Dr. Oyama is a member of the Magnetics Society of Japan and the Japan Biomagnetism and Bioelectromagnetics Society.

Masanori Higuchi received the B.S., M.S., and Ph.D. degrees from the University of Tsukuba, Tsukuba, Ibaraki, Japan, in 1986, 1988, and 1991, respectively.

Since 1995, he has been working at the Applied Electronics Laboratory, Kanazawa Institute of Technology, Ishikawa, Japan. His current research interests include biomagnetic measurements and data analysis.

Dr. Higuchi is a member of the Japan Biomagnetism and Bioelectromagnetics Society.

Gen Uehara (Member, IEEE) received the B.S., M.S., and Ph.D. degrees from The University of Tokyo, Tokyo, Japan, in 1979, 1981, and 1995, respectively.

From 1981 to 1986, he carried out research on Josephson junction as a Research Associate at the University of Tokyo. In 1986, he joined Yokogawa Electric Corporation and developed SQUID magnetometers and MSW oscillators. In 1990, he joined the Superconducting Sensor Laboratory to develop multichannel SQUID systems. In 1996, he became a Visiting Professor at the Kanazawa Institute of Technology, Ishikawa, Japan. Since 2007, he has been a Professor at the Kanazawa Institute of Technology. His current research interests include magnetoencephalograph, magnetocardiograph, and other applications of cryoelectronics.

Dr. Uehara is a member of the Japan Society of Applied Physics and the Japan Biomagnetism and Bioelectromagnetics Society.